

4

Cobalt Doped Nanostructured ZnO/p-Si Heterojunctions for Energy Conversion Devices

P. Hari* and A. Kaphle

Department of Physics and Engineering Physics
University of Tulsa, Tulsa, Oklahoma, OK 74104, USA

*Corresponding author

Outline:

Introduction	75
Experimental Methods	76
Absorption Studies	77
Morphological Studies	79
X-ray Diffraction	79
Photoluminescence Studies	80
Current-Voltage measurements	81
Capacitance-Voltage Measurements of Doped Heterojunctions	86
Variation of Electrical Impedance with Cobalt Doping	88
Discussion	92
Conclusions	94
Acknowledgements	94
References	95

Introduction

ZnO thin films have been deposited using number experimental techniques such as sputtering [1], spray pyrolysis [2], pulsed laser deposition [3], reactive evaporation [4], sol-gel method [5], solution based growth [6], and high temperature, and arcing in vacuum [7]. Using any one of the above deposition methods high quality ZnO thin films can be obtained on various substrates. Previous studies have shown that [8-10] transition metal doped ZnO thin films and nano particles exhibit novel structural, magnetic and optical properties. Typical absorption of ZnO is centered on UV light region of the solar spectrum due to its large bandgap. One of the important challenges in the fabrication of ZnO nanomaterials for solar energy applications is to tailor the optical properties of nanostructured films to absorb light in the visible range. We have developed a simple, low energy fabrication method for ZnO nanorods deposition on various substrates using a chemical bath deposition (CBD) technique [11-16]. CBD technique for fabricating ZnO nanorods can be easily adapted to incorporate metallic atoms during the growth of nanorods on various substrates at low temperatures. In this study we specifically focus on nanostructured ZnO thin films fabricated by a simple, low temperature and scalable CBD technique.

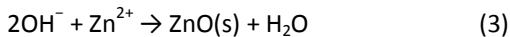
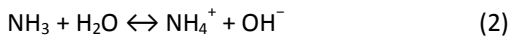
The CBD technique we used in this study is a modification of the original wet chemical technique proposed by Vysaiaress [17] in 2003. Since nanostructures can be modified relatively easily by changing deposition parameters such composition, pH values, temperature and deposition time, this technique can be easily modified to yield ZnO nanorods of various morphologies. Optical absorption and transport properties in nanostructures thin films crucially depend on morphologies of the underlying nanostructure. For this reason alone, it is important to fabricate nanostructured ZnO thin films instead of conventional thin films for optical wave guides and photovoltaic (PV) applications. The CBD technique adapted for ZnO nanorod deposition holds significant advantages over other solution based methods due to low temperature deposition process and scalability of the chemical bath process. In addition, it has been shown that [18-19] dopants such as Al, Ga, Cu and Cd can be added to ZnO structure which results in tuning of the optical band gap of the metallic doped ZnO film. Bandgap engineering is a very attractive process in PV materials where a wide band gap material such as ZnO with a bands gap of 3.37 eV can be controlled by incorporating metallic dopants. For example, Cobalt doped ZnO nanoparticle shows a decrease in bandgap, from 3.27 to 2.87 eV, [16] where as in Magnesium doped ZnO, the bandgap increased from 3.37 to 3.44 eV [20].

Nanostructured thin films deposited by CBD hold great promise for PV applications. The precise control of the growth parameters can be incorporated into the CBD process. Metallic doping to control bandgap can also be easily integrated into the precursor solutions of the CBD process. It has been also demonstrated that nanostructured ZnO of variety of morphologies can be grown on substrates such as p type silicon for PV applications [21]. In addition, doped nanostructured thin films can be fabricated by an inexpensive, low temperature CBD technique resulting in high quality electronic and optical properties comparable to thin films grown by chemical vapor deposition, spray pyrolysis and electrolysis techniques [22].

The main focus of this study is to characterize heterojunctions produced by cobalt doped ZnO nanorods deposited on p-Si by electrical, optical and structural methods. Specifically, I-V, C-V, and electrical impedance techniques were used to investigate heterojunction properties under external bias and annealing temperatures. Defects formed at the interface were investigated by modeling the impedance spectra with a parallel RC circuit.

Experimental Methods

Details of the sample preparation were published elsewhere [11-16] and will not be discussed in detail here. The CBD method used in ZnO nanorod deposition consists of a precursor solution made from zinc nitrate hexahydrate ($\text{Zn}(\text{NO}_3)_2 \cdot 6\text{H}_2\text{O}$) (ZNH), hexamethylenetetramine ($\text{C}_6\text{H}_{12}\text{N}_4$), and high purity (HP) de-ionized (DI) water. Substrates are suspended in the precursor solution at temperatures under 100 °C for 6-12 hours, depending on the desired nanorod morphology. The possible mechanism for producing ZnO nanorods by CBD is as follows: Thermal decomposition of the hexamethylenetetramine (HMT) releases hydroxide ions (OH^-), which react with the Zn^{2+} ions to form ZnO. The process for formation of ZnO can be explicated by the following chemical reaction [23]:



Undoped ZnO displays residual *n*-type conductivity, which has been attributed to native defects such as oxygen vacancies and interstitial zinc atoms, but also to uncontrollable hydrogen impurities introduced during growth that act as shallow donors. *n*-type doping of ZnO has been achieved by introduction of group-III elements such as Al, Ga, and In as substitutional atoms for Zn, and group-VII elements (Cl and I) as substitutional elements for Oxygen. Highly conductive *n*-type ZnO films have been demonstrated using group III elements as dopants [24]. Significant research has also been directed toward transition metal doping with elements including Co, V, Fe, Ni, and Mn to alter the magnetic and optical properties of ZnO. Among the transition metal dopants, cobalt has received considerable attention due to the attainment of room temperature ferromagnetism in Co-doped thin films [25].

Cobalt atoms can be easily introduced into ZnO with very little induced strain in the host ZnO lattice structure due to the similar ionic radii of Co^{2+} (58 pm) and Zn^{2+} (60 pm) ions. As a result, the Wurtzite structure of ZnO crystal remains unaffected by Cobalt doping. In addition to CBD, number of methods have been used for Co doping ZnO nanostructures, including sol-gel synthesis [26], pulsed laser deposition [27], and aqueous solution-based methods [28]. This study focuses on the properties of Co-doped nanorods grown by the hydrothermal solution method, again due to its simplicity, low temperature, and reduced cost compared to other techniques.

Cobalt doping concentrations ranging from 5–20 at. % were achieved by the introduction of cobalt nitrate hexahydrate ($\text{Co}(\text{NO}_3)_2 \cdot 6\text{H}_2\text{O}$) and cobalt chloride into the precursor solution consisting of equimolar concentrations of ZNH and HMT in high purity DI water. The doped precursor solution was then stirred for at least 2 hours before being filtered. Details of the preparation method can be found in previous published results [11-16].

Sputtered ZnO thin films were fabricated on glass and p-Silicon substrates using a DC sputtering system. ZnO seed layer was deposited by DC sputtering with pressure of 1.5×10^{-6} mbar and 120 W power using Zinc target and then annealed to get ZnO layer. The resulting films were 250-325 nm thick, and highly uniform. Photoluminescence (PL) measurements were taken of the Ar annealed thin films, using a Jasco FB 6500 spectrofluorometer with excitation wavelength of 325nm. PL intensity was measured for emission wavelength ranging from 350nm to 650nm. AC impedance measurements were performed using Bode 100 Omicron lab network analyzer for the frequency

range of 10 Hz to 5 MHz. Capacitance measurements were performed using a Keithley 590 C-V analyzer with a home-made bias configuration.

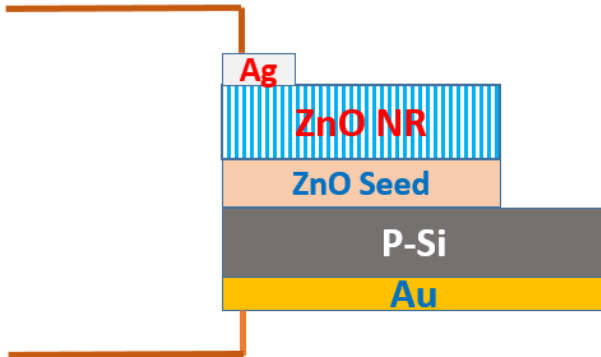


FIGURE 4.1
Structure of the p-Si/n-ZnO heterojunction used in this study

Figure 4.1 shows the basic design of the ZnO-p-Si heterojunction used in study. The deposition of a thin film ZnO seed layer on p-Si is achieved by DC sputtering. ZnO nanorods doped with Cobalt were grown by inserting the seeded substrate into the chemical bath.

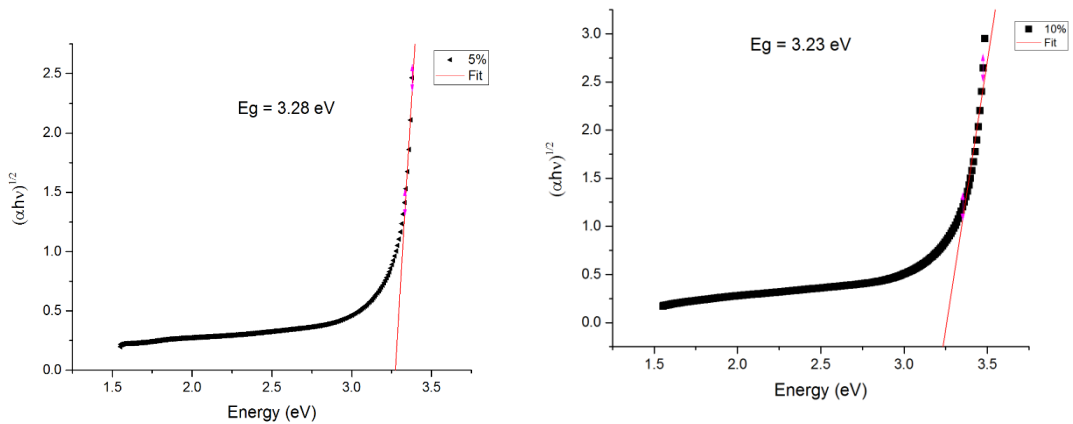
Absorption Studies

Five nanostructured ZnO samples with cobalt doping using CBD on p-Si were grown. The cobalt content was varied from 0-20% in these samples. Fig. 4.2 summarizes the optical absorption of ZnO nano structured thin films with doping.

Doping of transition metals such as cobalt is an efficient process by which we can tune the bandgap of a semiconductor such as ZnO. Cobalt and Mn are especially important because these dopants possess large magnetic moments. Doping with metallic ions also produces ZnO with low resistivity, which is an important consideration for solar cells and transparent conductors. The direct bandgap of films was extracted from the absorption vs. energy. Using the Tauc relation adapted to direct bandgap semiconductors:

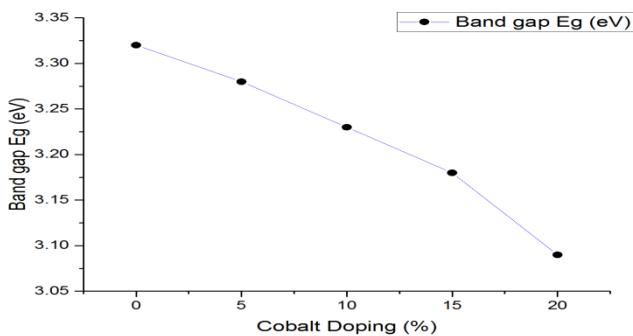
$$\alpha hv = C (hv - E_g)^{1/2} \quad (4)$$

where α is the absorption coefficient, C is a constant, ν is the optical frequency and E_g is the optical bandgap. As shown in Figure 4.2, the optical bandgap decreases with cobalt doping. Absorption data for doped ZnO shows a systematic decrease in optical band gap with doping concentration as shown in Figure 4.3. The Previous studies of low level of doping concentrations [29] in ZnO nanoparticles doped with cobalt indicated that optical bandgap increased for 1% cobalt while the optical bandgap decreased when the cobalt doping increased from 1 -2% in

**FIGURE 4.2**

Absorption vs. Energy measured for 5 and 10% cobalt doped ZnO nanostructured films

cobalt doped powdered samples. Reduction in bandgap could be due to confinement of electrons in nanoparticles. In the case of ZnO we observe uniform morphology in nanorods. A decrease in bandgap with Manganese doping in ZnO has been also observed in previous studies [30]. The observed decrease in bandgap with cobalt could be due to strong exchange interaction enhanced by the doping of magnetic ions such as cobalt. Doping with transition metallic ions such as Cobalt and Manganese result in facilitating exchange interaction between p and s electrons of the ZnO atoms with the d electrons of the transition metallic ions. One important consideration is that the exchange interaction is present even in the absence of external magnetic field. Previous studies of cobalt doped polycrystalline ZnO thin films also showed a decrease in bandgap [31]. During cobalt doping, we also observe from SEM images that the average ZnO nanorod diameter increases as the doping is increased from 0- 20% as shown in Figure 4.3. However, we did not observe any significant changes lattice parameters with doping using x-ray analysis. Energy dispersive x-ray measurements of doped ZnO nanorods did not reveal the presence of cobalt in heavily doped ZnO nanorod samples. This is in sharp contrast with significant morphological changes and lattice parameter variations observed in ZnO nanopowders doped with cobalt [32].

**FIGURE 4.3**

Band gap energy vs cobalt doping concentration for ZnO nanorods

Morphological Studies

We used scanning electron microscopy (SEM) to study morphological variations in cobalt doped ZnO. Figure 4.4(a-d) shows the SEM images of 5-15 % cobalt doped ZnO nanorods deposited on p-Si.

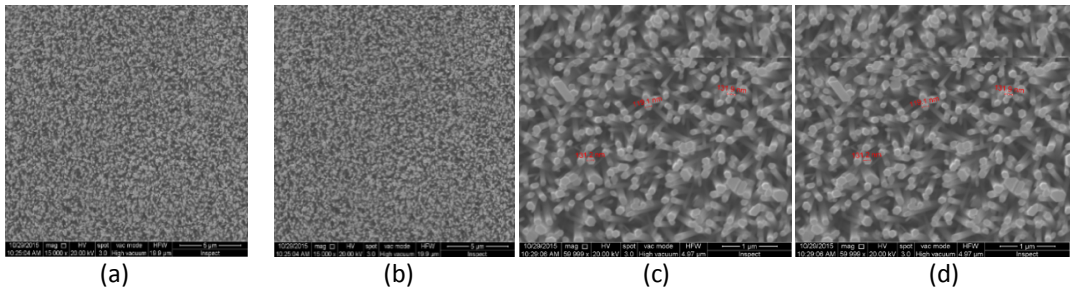


FIGURE 4.4

Figures (a) and (b) show the SEM images of ZnO nanorods with 5 % and 10 % cobalt doping. Figures (c) and (d) show a selection of graph (a) and (b) magnified 15,000x from images taken in (a) and (b). The red markings on images (c) and (d) are used to measure diameter of nanorods

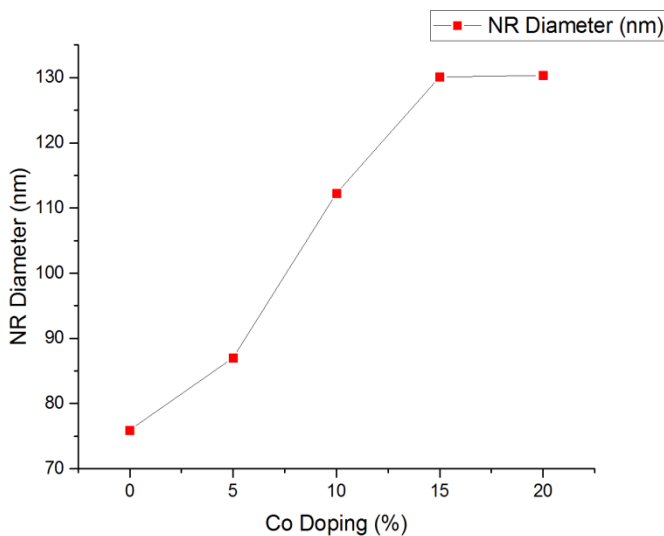


FIGURE 4.5

Increase in ZnO nanorods diameter with doping concentration from SEM analysis

X-ray Diffraction

Figure 4.6 shows the regular x-ray spectra for doped and undoped ZnO nanostructured films. It is important to notice that cobalt incorporation in other morphologies of ZnO resulted in a reduction of X-ray diffraction intensity [33]. Typical X-ray ZnO nanorods films do not show any measurable

difference between doped and undoped films. In addition, we did not observe any indication of Cobalt oxygen complexes in x-ray spectra even at high doping concentration of 20%. We observed sharp and intense X-ray reflection along (002) in all doped samples indicative of highly oriented crystalline structure in these samples. We did not observe any changes in lattice parameters even in samples as high as 20% cobalt doping. This result is in sharp contrast with increases in lattice constants cobalt doping observed in thin film ZnO samples [34].

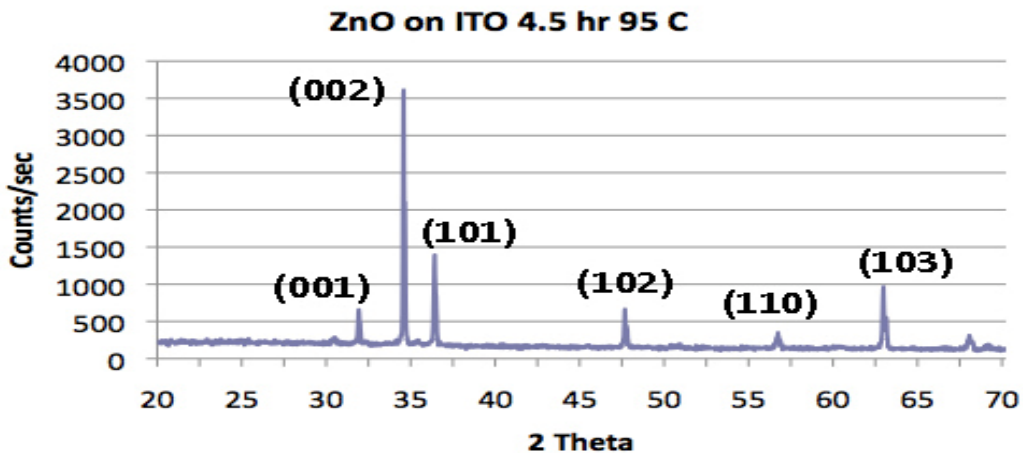


FIGURE 4.6
Typical x-ray spectra of a nanostructured ZnO film

Photoluminescence Studies

We investigated changes in the photoluminescence (PL) spectra of cobalt doped ZnO nanorods. The full PL spectrum of samples is shown in Figure 4.7. The PL spectrum show characteristic peaks related to impurities centered around 475 nm and oxygen vacancies centered around 575 nm. Our results show that the UV emission peaks in cobalt doped thin films at 392 nm (3.17 eV) which corresponds to near band emission (NBE) of undoped ZnO, is not affected by doping. Even at high dopant concentration, there is no shift in the NBE peak. This is consistent with the observed x-ray data that the Wurtzite structure and lattice parameters are not significantly affected by cobalt doping. This result is in sharp contrast with red shift in UV near band edge emission observed in ZnO nano particles doped with cobalt [35]. PL spectrum in Fig. 4.6 shows several features in the visible and near infrared region.

The samples examined in the PL studies were post annealed at 150°C for 2 hrs in air. The PL emission peak around 488 nm is generally indicative of oxygen vacancies. As shown in Fig. 4.6, the PL peak at 488 nm is significantly enhanced by cobalt doping. The green emission observed around 560 nm is indicative of oxygen vacancies present in the samples. As the cobalt doping percentage is increased, the green band emission at 560 nm is significantly enhanced. ZnO nanoparticles doped with other transition metals such as Mn [35] show similar effects in the PL peak near 560 nm attributed to oxygen vacancies. As shown in Fig. 4.6 the peak of the PL spectrum shows a slight blue shift with doping as the doping concentration is increased from 0 to 20%. In the context of bandgap

narrowing with doping, it was suggested that the magnetic interactions resulting from s-p and p-d coupling from cobalt doping may be a possible mechanism for lowering of the bandgap. These interactions involving s-p and p-d states could give rise to coupling between extended band tail states. This in turn could give rise to shift in conduction band oxygen related vacancies towards higher energy. As the doping concentration is increased, it is very likely that the transition probabilities to oxygen and zinc related states become energetically favorable. It is interesting to note that even at high doping concentration the NBE peak corresponding to excitons is not shifted in energy. This could be an indication of the overall quality of the thin film samples as well as the absence of non-radiative transitions mediating the recombination process in cobalt doped ZnO films. We also performed post annealing studies of samples doped with cobalt. We observed that above 600 C the UV peak decreases significantly in doped samples. This could be another indication that defects are formed at high temperature and non-radiative transitions are becoming the favorable process for recombination as the quality of the samples degrades upon annealing.

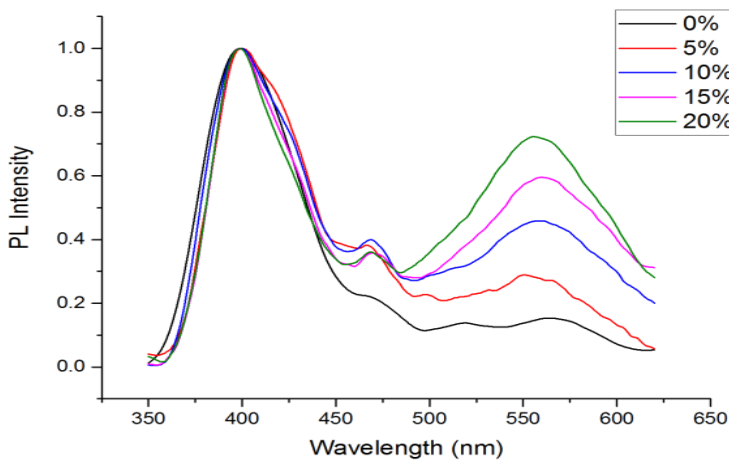


FIGURE 4.7
PL spectrum of cobalt doped nanostructured ZnO films

Current-Voltage measurements

Figure 4.8 shows the I-V characteristics of the p-Si/ZnO heterojunction under illumination (a) and dark (b) condition. It is evident from the I-V data shown below that the p-n junction shows strong rectification properties with doping under both dark and illumination condition. One notable feature of the I-V curves with doping is that the current increases with forward bias up to 15% doping, but abruptly decreases after 15%. As the bias voltage is increased, the slope of the I-V curve appears to change at about 3V. The deviation from linear increase in semi log plot of I vs V is characterized by higher power in the current voltage exponent. This in turn could be an indication of the space charge limited conduction processes in heterojunctions [36].

As shown in the Figures 4.8 a) and b), the current increases with doping concentration in illumination and dark conditions. From the standard diode equation:

$$I = I_0 (\exp (qV/nKT) - 1) \quad (5)$$

where q is the charge, V is the voltage, K the Boltzmann's constant and T is the temperature in Kelvin. We extracted the diode ideality factor from the log of the slope of the I-V curve. The ideality factor equation is given by;

$$n = q / (kT * \text{Slope of I-V curve}) \quad (6)$$

Figure 4.9 shows the variation in the ideality factor estimated with various doping levels.

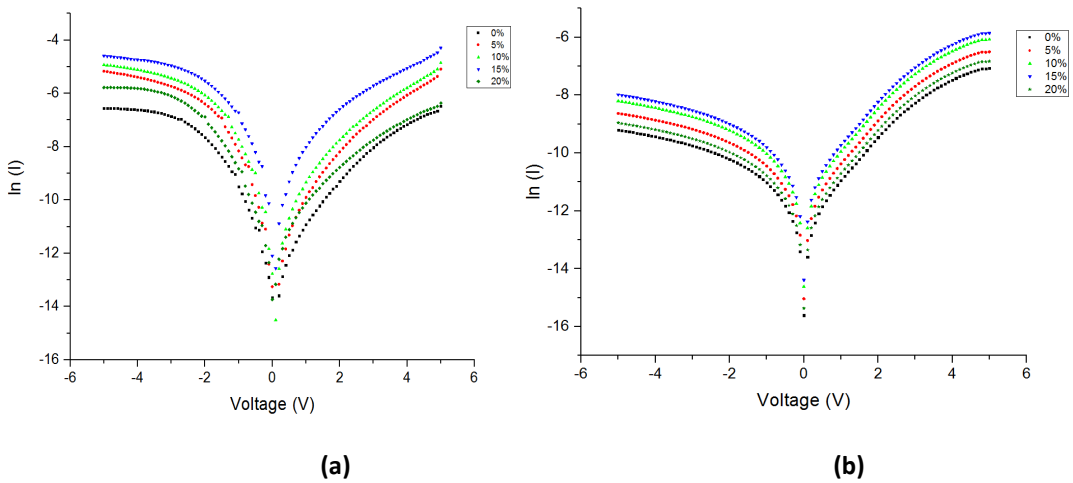


FIGURE 4.8

Current voltage measurements of cobalt doped p-Si heterojunction under (a) illumination and (b) dark are shown

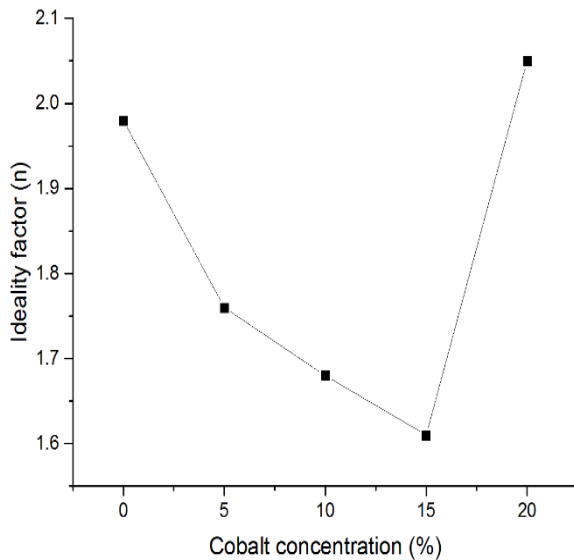


FIGURE 4.9

Variation of Ideality factor with Cobalt concentration

Typically, ideality factor is about one for a p-n junction at low voltage. The ideality factor extracted from the p-Si/ZnO shows a dramatic decrease from 2 to 1.6 as the doping is varied. As shown in Fig. 4.9, the ideality factor again increases from 15 to 20% doping. Increasing in ideality factor is an indication of the recombination process taking place in the p-n junction. As the doping is increased beyond 15%, rapidly rising ideality factor shows that the ideality factor is not stabilized. This may be an indication of the changing recombination rate or the degradation of the junction as the doping is increased beyond 15%. Increase in the diode ideality factor is quite significant for doping above 15%. Since recombination is enhanced by defects, higher occurrence of defects with doping could lead to enhanced space-charge recombination. In the I-V measurements a drop in current shown in Fig. 4.8 at higher doping levels is consistent with a higher recombination rate taking place in 20% cobalt doped p-Si/ZnO heterojunction.

Analysis of I-V vs Temperature for Doped ZnO Heterojunction

We investigated the changes in I-V characteristics of the ZnO doped samples annealed at temperatures varying from 300-420K. As the temperature is varying we can write the diode equation described above (Eqn. 6) as

$$I = I_0(T) (\exp (qV/nKT) - 1) \quad (7)$$

where the saturation current I_0 is a function of temperature. The temperature-dependent saturation current can be related to the effective barrier height ϕ_{b0} by the relation:

$$I = I_0(T) AA^*T^2 \exp (q\phi_{b0}/kT) \quad (8)$$

where, A and A^* are the contact area and Richardson constant respectively and ϕ_{b0} is the effective barrier height.

Taking the natural log of Eqn. 8 we obtain

$$\ln(I_0/T^2) = \ln (AA^*) - q\phi_{b0}/kT \quad (9)$$

$\ln(I_0/T^2)$ vs q/kT plot gives barrier height and Richardson constant from slope and intercept. The value obtained for Richardson constant is very low as compared to theoretical values $32 \text{ A cm}^{-2} \text{ K}^{-2}$. This deviation of Richardson constant is may be due to barrier in homogeneity at junction interface. This fluctuation is modeled by Gaussian distribution of barrier height with standard deviation σ_0 and average barrier height $\overline{\phi_{b0}}$ [38 - 39] can be expressed as

$$\phi_{b0} = \overline{\phi_{b0}} - q\sigma_0^2/2kT \quad (10)$$

The modified Richardson equation is,

$$\ln(I_0/T^2) - q^2\sigma_0^2/2k^2T^2 = \ln (AA^*) - q\overline{\phi_{b0}}/kT \quad (11)$$

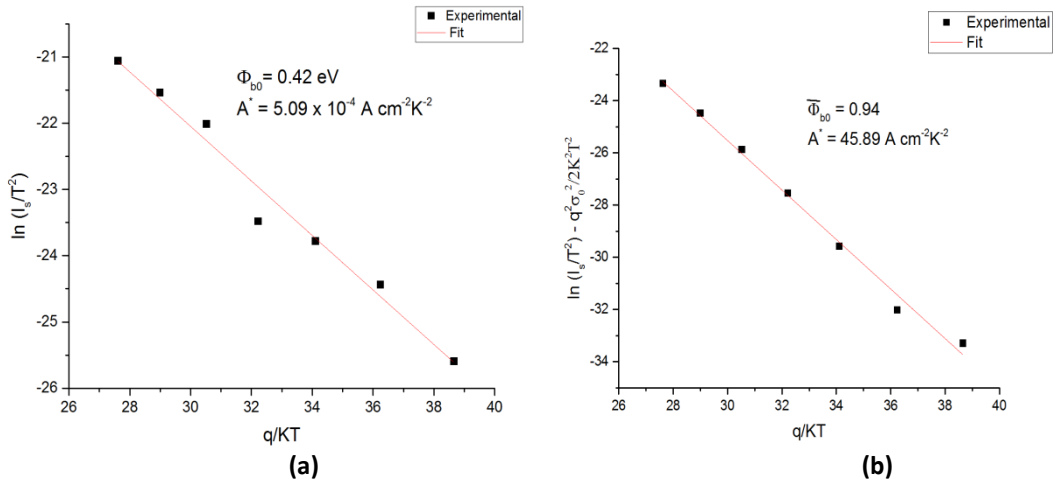


FIGURE 4.10

(a) Richardson plot (b) Modified Richardson plot for 0% Co for the temperature range of 300K – 420K

The plot of $\ln(I_0/T^2) - q^2\sigma_0^2/2k^2T^2$ vs q/kT is a good fit to a straight line in which slope and intercept gives average barrier height and the Richardson constant respectively. By considering barrier height inhomogeneity and applied modified Richardson equation we obtain the Richardson constant value very close to theoretical value. Figure 4.10 shows the Richardson plot (Fig 4.10 a) and the modified Richardson plot based on Eqn. 11 (Fig. 4.10 b).

Similar procedure was employed for other doped samples. Table 4.1 summarizes the extracted average modified barrier height from all samples. From Table 4.1 it is clear that the barrier height is modified by cobalt doping up to 15% doping. As the doping level is increased to 20%, the barrier height increasing trend is broken and the barrier height abruptly reduces to a value below the estimate for the undoped ZnO. This may be due to the increase in defect mediated recombination taking place at 20% cobalt doping level in the material.

TABLE 4.1

Estimation of barrier height from the modified Richardson equation

Co %	Barrier height (eV)
0	0.94
5	0.99
10	1.05
15	1.12
20	0.91

We also analyzed the I-V curve for doped samples by estimating the rectification ratio (RR) from 300 K -420 K. Fig. 4.11 shows the RR values estimated from the absolute current through the heterojunction at +/- 3V. There is an increase in RR with doping up to 15% doping level and then RR

drops to a lower value at 20%. This trend is again consistent with the reduction in ideality factor and barrier height in n-ZnO/p-Si heterojunction at 20% cobalt doping level.

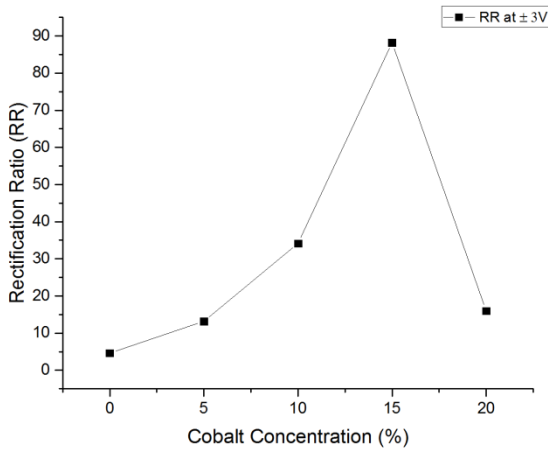


FIGURE 4.11

Rectification ratio vs doping level in various samples at $\pm 3V$

We investigated the variation in rectification ratio with annealing temperature for doped samples. Fig. 4.12 shows the changes in RR with temperature. As shown in Fig. 4.12, there is systematic increase in RR with temperature as the doping is varied to 15%. At 20% doping level, again there is an abrupt drop in the RR value. The observed increase in RR with temperature is consistent with a series resistance model [40] used in analyzing changes in RR in heterojunctions formed with ZnO with temperature. The observed increase in RR with temperature up to 15% doping could be indicative of a single dominant resistive channel in mediating transport. As the doping level increases beyond 15%, the presence of defects reduced the conduction via series resistance and thus lowering the RR value in 20% cobalt doped ZnO/p-Si sample.

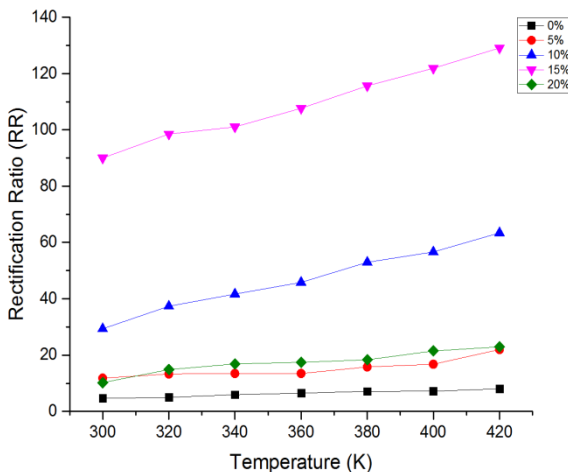


FIGURE 4.12

Variation of rectification ratio with temperature in doped heterojunctions

Capacitance-Voltage Measurements of Doped Heterojunctions

Further investigations of electrical properties were performed by measuring the capacitance voltage (C-V) variations in the doped ZnO-p-Si samples. C-V measurements were performed at 100 KHz using a Keithley C-V analyzer. The relation between capacitance and bias voltage relates two important parameters for the ZnO-pSi heterojunction. We used the relation

$$(A/C)^2 = -2(V_{bi} - V)/q\epsilon_0\epsilon_r N_d \quad (12)$$

for estimating the built-in potential V_{bi} and the dopant density N_d . In Eqn. 12, we used the value of the dielectric constant ϵ_r for ZnO as 9 and the density of the conduction band states from the literature [41] as $N_c = 4.8 \times 10^{18} \text{ cm}^{-3}$ for ZnO. The effective cell area, A of each sample was $7.8 \times 5.3 \text{ mm}^2$. The dopant concentration N_d in various samples was estimated from the equation

$$N_d = -2/q\epsilon_0\epsilon_r (\text{slope of } 1/C^2 - V) \quad (13)$$

Figure 4.13 (a) and (b) show the raw C-V data and the plot of $(A/C)^2$ vs V for various doped samples.

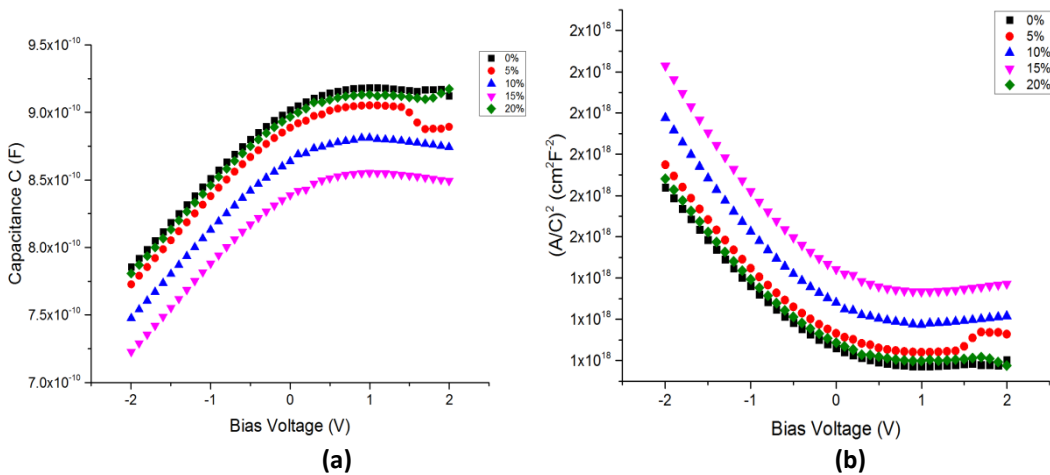


FIGURE 4.13 C-V (a) and $1/C^2 - V$ plot (b) for cobalt doped samples

The barrier height ϕ_b in a heterojunction is related to the built-in voltage V_{bi} by a relation given in Eqn. 14.

$$\phi_b = V_{bi} + kT/q \times \ln(N_c/N_d) \quad (14)$$

where V_{bi} is the built-in voltage, N_c and N_d are the conduction band density of states and dopant concentration respectively.

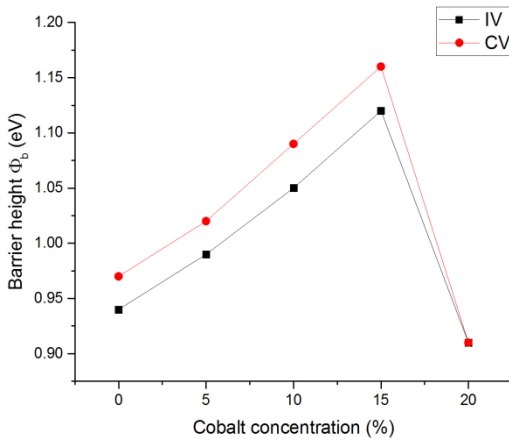


FIGURE 4.14
Barrier height comparison from I-V and C-V analysis

Figure 4.14 compares that barrier height estimations based on previous I-V measurements (Table 4.1) and the C-V measurements. These two measurements yield similar values and the trend with doping concentration is the same using two different measurements. As indicated before, the built in voltage increases with doping till 15% doping concentration. Both C-V and I-V measurements indicate that the drastic reduction in the barrier height at 20% doping. It is interesting to note that the barrier height at 20% drops to a level below the undoped ZnO sample. This could be an indication of the

Depletion Width and Carrier Concentration from C-V Data

Figure 4.15 (a) shows the depletion width extracted from the data represented in Fig. 4.13 (b). The built-in voltage V_{bi} and the doping concentration N_d can be directly extracted from the extrapolation of the $1/C^2 - V$ data shown in Fig. 4.13 b.

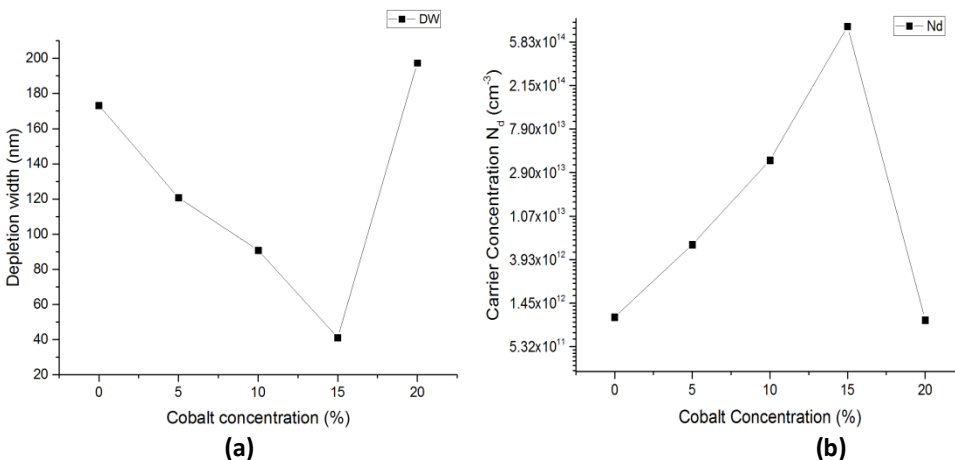


FIGURE 4.15
(a) Depletion width (b) and carrier concentrations extracted from C-V measurements of Co-ZnO/p-Si heterojunction

As the doping level increases, the depletion width is reduced from 0.18 microns to 0.040 microns. Both built-in voltage and doping concentration shows the abrupt variation different from the trends followed up to 15% doping. These results are again consistently showing the anomalous values of junction parameters at 20% cobalt doping could be due to defects mediating the recombination process.

Variation of Electrical Impedance with Cobalt Doping

In nanomaterials made of nanorods and nanowires there many defect states arising from dangling bonds on surfaces, vacancies and grain boundaries. These defect states significantly influence transport properties in nanostructured materials. One proven technique for probing the defect states is by impedance spectroscopy. Since the surface to volume ratio is significantly large for nanostructured materials compared to the bulk, the impedance measurements in these materials will be heavily influenced by gran structure and grain boundary states [42, 43].

Transport properties of ZnO nanorod-nSi heterojunction were investigated using impedance spectroscopy. By plotting the impedance of a circuit element with a capacitor and resistance in parallel, with frequency we can obtain the effective resistance and capacitance of a crystalline unit. Impedance of a simple resistance-capacitance in parallel is given by:

$$Z = \{ [1/R + j\omega C] \}^{-1} \quad (15)$$

By plotting the real and imaginary component of the impedance function, we can extract contributions from grains within a crystalline unit, resistance and capacitance between two grain boundaries. Figure 4.16 shows the imaginary vs real component of the impedance for n-ZnO/P-Si heterojunction as the doping is varied. From the real part of the impedance data, we extracted the resistance for each ZnO sample doped with cobalt (Fig. 4.16 (b)). As the doping is increased, the resistance rapidly decreases with doping. This could be viewed as the bulk or series resistance across the doped semiconductor. Thus the reduction in resistance is consistent with higher level of doping because of the movement of the Fermi energy towards the conduction band with increase in doping concentration.

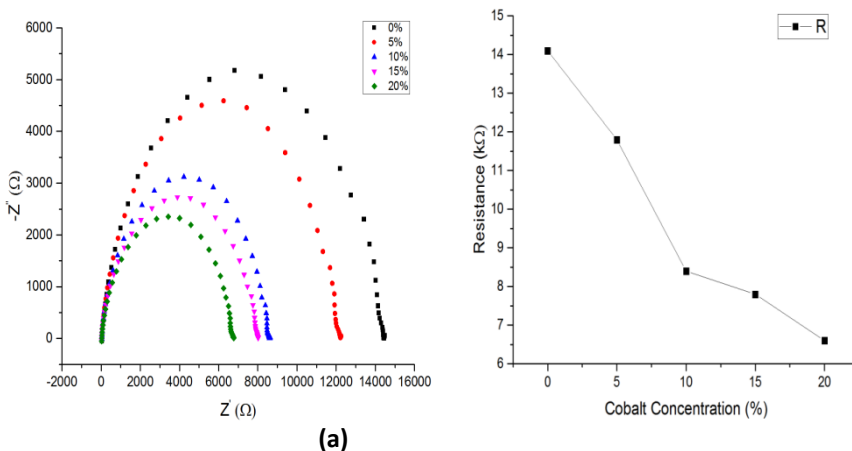


FIGURE 4.16

(a) Nyquist plot for different cobalt Concentration (b) variation of resistance with doping

Impedance Measurements Under Annealing Conditions

We performed impedance measurements on doped ZnO/p-Si annealed from 100 C to 400 C. Two typical data sets for an undoped and doped sample are shown in Fig. 4.17. Transport properties in the doped samples were investigated by measuring the real and imaginary parts of the impedance function. Nyquist plots at various temperatures can provide detailed information on transport properties of grains and grain boundaries.

If we assume a simple circuit element consisting of a resistor and capacitor in parallel for each grain, grain interface and grain boundary, within the material, we can attribute a thermally activated relaxation time τ for each region given by

$$\tau = \tau_0 \exp (E_a/KT) \quad (16)$$

E_a is the thermal activation energy, K is the Boltzmann constant and τ_0 is the pre exponential factor [44]. Figure 4.17 a and b are representative of the temperature variations in doped ZnO heterojunctions. It is important to notice that the size of the semicircle decreases as the temperature is increased to 400 C. We observe a well-defined single semicircle from 100 C to 400 C in doped ZnO samples. This is in sharp contrast with multiple semicircles observed in undoped ZnO nanotubes reported by previous studies [42, 43]. In general we can assume two separate and distinct time constants for the grain and grain boundaries within the nanomaterial. The transport process through the grain and grain boundaries can be modeled by a simple parallel circuit elements made of $R_g, C_g, R_{gb},$ and C_{gb} [45, 46], where the subscripts correspond to resistance and capacitance for grain and grain boundaries of the nano material. Fig. 4.18 illustrated the simple circuit element made of a¹ used in analyzing the Nyquist plot at temperatures in various cobalt doped heterojunctions. R_s , the resistance in series in the circuit element of Fig. 4.18 denotes the contact resistance between the ZnO nanorods and the electrodes used for impedance measurements.

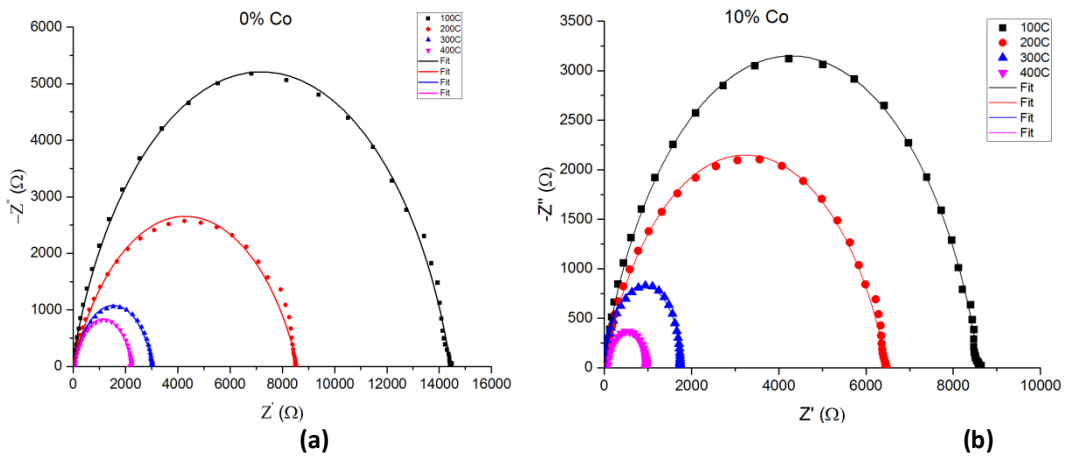


FIGURE 4.17
Nyquist plot of (a) 0% Co (b) 10% Co with temperature

The Cole –Cole modifications of the Debye equation can be adapted to analyze the impedance vs temperature data based on the model described in Fig. 4.18

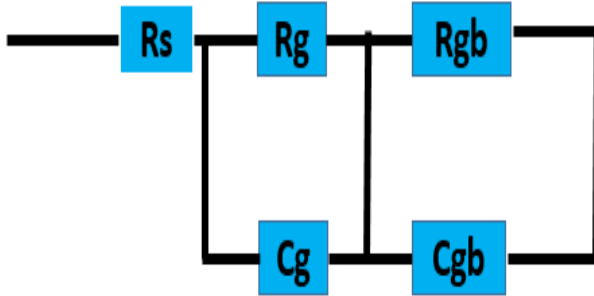


FIGURE 4.18
RC circuit model for impedance modeling

The complex impedance $Z(\omega)$ can be analyzed by the expression

$$Z(\omega) = Z_r - Z_i(\omega) \quad (17)$$

where Z_r and Z_i are the real and imaginary parts respectively. We can extract the transport parameters by calculating the complex impedance. If we use fitting parameters as the real axis intercepts R_1 and R_2 from each Nyquist plot. The Nyquist plot can be modeled as two intersecting semicircle contributions with R_3 and the third parameter corresponding to the overlapping intersection point of the two semicircles. Based on these parameters a model was developed for fitting the impedance data [44]. The impedance function used in our curve fitting is:

$$Z(\omega) = R_s + (R_2 - R_1)/(1+j\omega\tau_g) + (R_3 - R_2)/(1+j\omega\tau_{gb}) \quad (18)$$

where the relaxation times for the grain and grain boundary are given by $\tau_g = C_g R_g$ and $\tau_{gb} = C_{gb} R_{gb}$ respectively. Table 4.2 describes the parameters for the grain and grain boundaries extracted using this model.

As shown in Table 4.2, we can extract thermal activation energy for the grain and grain boundary relaxation process. Fig. 4.19 a shows the thermal activation energy obtained for the sample at zero % doping for the grain and grain boundary.

TABLE 4.2

Transport parameters extracted from the impedance model

Co %	Temp (°C)	R_s (Ω)	R_g (Ω)	R_{gb} (Ω)	C_g (nF)	C_{gb} (nF)	τ_g (μ S)	τ_{gb} (μ S)
0%	100	44.45	7106.80	6915.50	0.14	0.62	1.01	4.30
	200	40.01	5305.14	3344.90	0.17	1.13	0.91	3.78
	300	34.22	1578.04	1325.60	0.42	1.84	0.66	2.43
	400	28.4	1105.30	821.34	0.51	2.33	0.57	1.92
5%	100	41.32	6401.16	5403.73	0.18	0.80	1.21	4.33
	200	32.63	5065.13	3007.76	0.21	0.87	1.05	2.61
	300	30.00	1038.37	740.42	0.46	1.02	0.47	0.75
	400	23.99	847.70	592.82	0.51	1.16	0.43	0.68
10%	100	41.01	4290.50	4198.53	0.29	1.07	1.26	4.49
	200	34.06	3829.52	2499.60	0.32	1.37	1.22	3.42
	300	26.11	968.60	631.66	0.38	4.06	0.37	2.56
	400	26.43	614.31	475.17	0.45	4.41	0.27	2.09
15%	100	40.92	3997.80	3851.33	0.43	2.99	1.71	11.51
	200	41.14	3156.40	2128.91	0.47	4.62	1.48	9.83
	300	27.24	641.03	502.09	0.85	5.92	0.54	2.97
	400	23.97	426.03	238.98	0.93	7.29	0.39	1.74
20%	100	37.81	3615.21	2986.41	0.81	4.24	2.95	12.66
	200	29.29	2995.14	2025.52	0.89	5.57	2.68	11.28
	300	28.86	725.97	486.80	1.03	4.45	0.74	2.16
	400	23.84	233.56	210.33	1.32	8.89	0.30	1.86

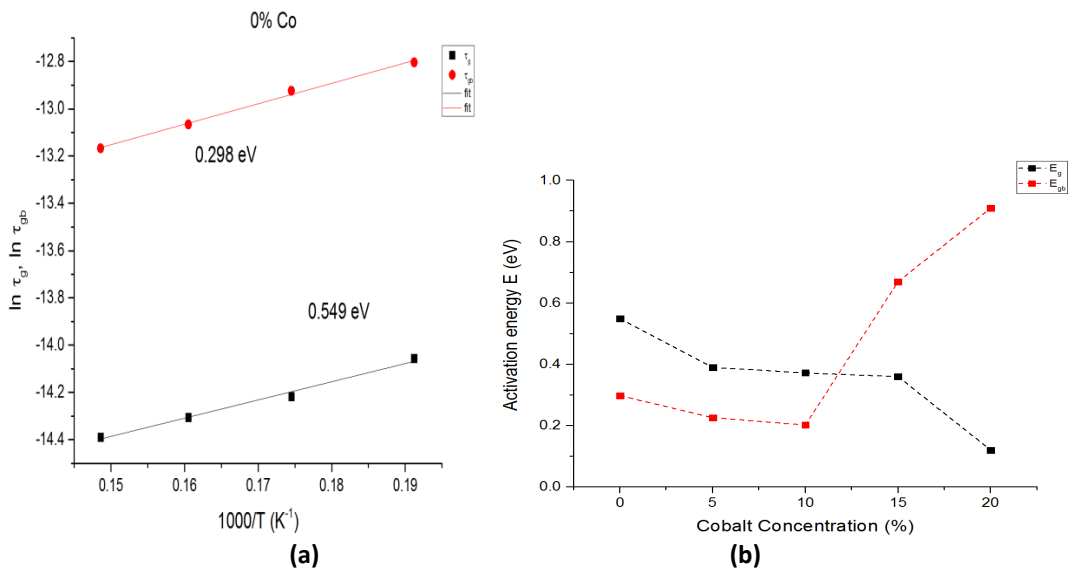


FIGURE 4.19

(a) Arrhenius plot 0% Co (b) Variation of Activation energy with Cobalt doping calculated from relaxation time

Fig. 4.19 b shows the overall trend in the activation energy with doping. Fig. 4.19 b shows that the activation energy for the grain boundaries increase as the doping level increases. However, the overall activation energy is reduced within the grains as the doping is increased. As the doping level increases, the deep donor levels within the bandgap are thermally activated and they contribute to the transport process at higher doping levels. It is interesting to note that the capacitance at the grain boundaries also increases with temperature. Charges are transported at higher rates as dopants are thermally activated. This increase in rate is reflected in the overall trend of increasing C_{gb} at higher doping levels. This increase in capacitance is accompanied by higher current and lower R_{gb} . Thus the overall relaxation time constant decreases at higher temperature and doping concentration.

Discussion

We investigated the optical, morphological and electrical properties heterojunctions made from n-ZnO and p-Si. Cobalt doped ZnO/p-Si heterojunctions can be tuned to have bandgap ranging from 3.32 eV (undoped) to 3.09 eV (Fig. 4.3). This is consistent with the magnetic interactions present in ZnO doped with magnetic ions such as cobalt.

The reduction in ZnO bandgap with cobalt doping can be explained as due to sp-d exchange interaction between localized d electrons of cobalt ions substituting for Zn ions.

The optical properties from PL show a steady increase in the impurity related peaks at 475nm as cobalt is introduced into the structure. We also observe an increase in oxygen related peak (Fig. 4.7) around 575 nm. X-ray results show that the structural parameters are minimally affected by cobalt doping. This could be an indication that cobalt is added to the structure interstitially rather than attached to the oxygen complex.

One of the important results in this study is the demonstration that beyond 15% doping, many of the junction characteristics degrade. Electrical measurements (I-V and C-V) used in this study show that cobalt incorporation is improving the rectifying properties as the doping is increased up to 15%. However, by comparing the junction parameters at 20% cobalt doping to C-V and I-V data obtained at lower doping levels we observe that the junction properties (Fig. 4.9) such as the ideality factor and rectification ratio (Fig. 4.12) degrade as more and more cobalt is introduced into the ZnO structure.

One important tool in characterizing the correlation between transport properties and structural properties is by impedance spectroscopy. Impedance measurements (Fig. 4.16) on various doped samples show that the series resistance of the material decreases with increased concentration of doping. This could be the indication that the Fermi levels is moving close to the conduction band as doping level is increased.

Impedance studies also show that impedance can be modeled by a simple R-C circuit. From the modified dispersion model [45] we can extract the transport parameters such as relaxation time constant for the grains and grain boundaries within the material. The parameters extracted (Table 4.2) from the modified dispersion yields several trends. The overall resistance of the grains and the grain boundary decreases with higher temperature. The thermal activation energy of the grains and grain boundary states show opposite trends with increased doping. As the doping levels are increased, the thermal activation within the grain is reduced. As discussed earlier this could be an indication that deeper donor levels are activated. At the grain boundaries we obtain large activation energies from our model. The relaxation time at the grain boundaries also show a steady increase with doping. As the temperature is increased, the relaxation time attributed to the grain

boundaries decrease in doped heterojunctions. This could be due to hopping transport taking place in the material.

From impedance data analysis we can get values of capacitance for grain and grain boundary and from this average capacitance of the circuit can be calculated. Fig. 4.20 shows the impedance data on various doped samples taken at forward and reverse bias. From the capacitance data with applied bias a plot of C-V and the $1/C^2 - V$ data similar to that of CV analysis in Fig. 4.13 b yield an estimate of the barrier height from impedance measurements. Table 4.3 summarizes the barrier height estimates obtained from the three electrical measurements in this study.

Table. 4.3 shows that the numbers and the trends are quite similar. As we observed from the doping dependence of doping and temperature, the junction properties, especially the built in voltage degrades at doping levels beyond 15%.

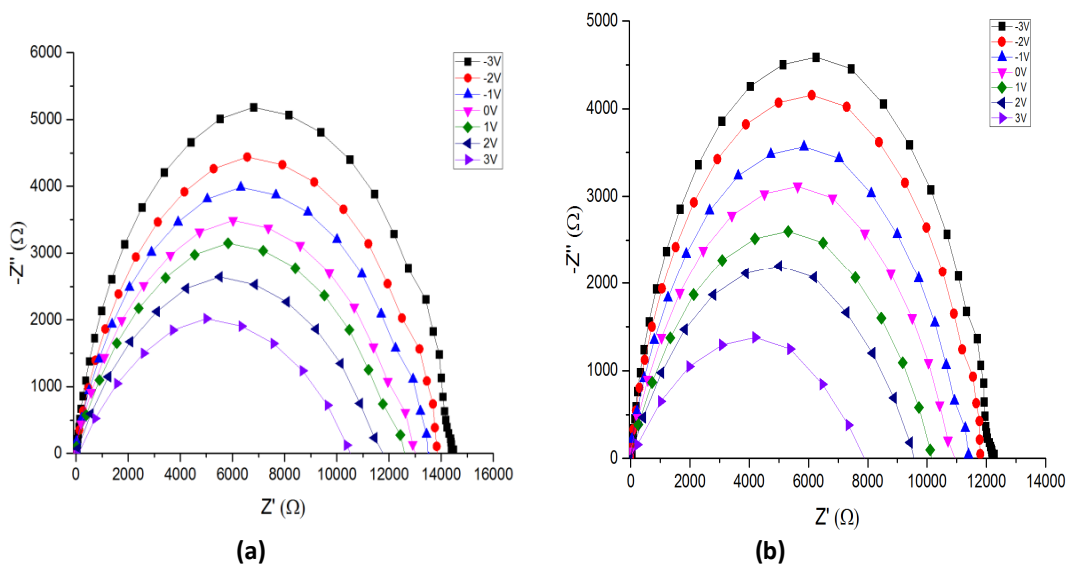


FIGURE 4.20 Nyquist plot of pSi-ZnO heterojunction under bias voltage -3V to +3V (a) 0% Cobalt (b) 5% Cobalt

TABLE 4.3 Barrier height estimates from I-V, C-V and Impedance measurements

Cobalt %	Barrier height (eV)		
	I-V	C-V	Impedance
0	0.94	0.97	0.90
5	0.99	1.02	1.09
10	1.05	1.09	1.13
15	1.12	1.16	1.17
20	0.91	0.91	0.84

The barrier height estimates from three methods are quite similar and the trend again shows that beyond 15% doping levels there is abrupt drop in the barrier height indicating the influence of defect mediated recombination processes taking place at higher doping concentrations.

Conclusions

Cobalt doped ZnO nanostructures were grown using chemical bath deposition method on p-Si doped with Boron. Investigations of the optical, structural and electrical properties reveal a significant variation in bandgap, absorption and impedance characteristics of the heterojunction.

Optical absorptions studies on the heterojunctions show that the optical bandgap in ZnO thin films decrease with increase in cobalt doping. Bandgap reduction with doping could be attributed to exchange interaction between p and s electrons of the ZnO atoms and the d electrons of cobalt ions. Photoluminescence (PL) studies at room temperature on heterojunction reveal PL peaks at 392 nm, 475 nm and 575 nm, typically attributed to near band (NB) emission, zinc vacancies and oxygen related vacancies in ZnO. As doping is increased, we observed no shifting or reduction in NB emission intensity, indicating that the Wurtzite structure is preserved under cobalt doping. Post annealing of ZnO after deposition of thin films at temperature of 600 C reveal that near band emission peak decreases in doped samples. This could be an indication of the structural defects formed as cobalt is diffusing out of the bonded sites.

Electrical measurements such as current-voltage (I-V), capacitance –voltage (C-V) and AC impedance measurements reveal properties if the junction degrading above 15% cobalt doping. I-V measurements on cobalt doped p-Si reveal deviation from linearity above 15% cobalt doping. This could be an indication of space charge limited conduction process taking place in heavily doped heterojunctions. In addition, I-V measurements reveal a sharp increase in the diode ideality factor above 15% doping. This effect could be an indication of the higher recombination rates in heavily doped heterojunctions. Our analysis of the I-V data on cobalt doped ZnO samples indicates a significant distribution in barrier heights with doping. C-V measurements also show that barrier height also decreases above 15% doping. Extraction of depletion width and carrier concentration of dopants from C-V measurements show a reduction in both parameters as the doping level is increased beyond 15%. These conclusions are consistent with the decrease in the rectification ratio above 15% cobalt doping in ZnO-p/Si heterojunctions. Ac impedance measurements also show a systematic decrease in series resistance and junction resistance with doping concentrations. Further, temperature variation of impedance was fitted with a simple capacitance-resistance model. Transport parameters such as resistance of the grains and grain boundaries reduce as the temperature is increased. This effect again could be an indication of the overall reduction in the relaxation time constants at higher levels of doping and temperature.

In summary, ZnO-p/Si heterojunction properties can be optimized by doping with transition metals such as cobalt. The electrical, structural and optical properties can be adjusted by a deposition process such as the chemical bath deposition method in precisely controlling doping concentrations.

Acknowledgements

The authors would like to thanks the funding agencies OK-NASA EPSCoR (project number NNX13AN01A and NNX15AM75A) and DOE ARPA-E for financial support. This work was also supported by the TU nanotechnology and the Oklahoma Photovoltaic research institute. Authors would like to thank collaborators Dr. K. Roberts (University of Tulsa), Dr. A. Apblett, Dr. N. Materer (Oklahoma State University) and Dr. I. Sellers (University of Oklahoma) for various fruitful

discussions and suggestions. We also acknowledge assistance in data processing from Ms. Echo Adcock Smith and Dr. Alexei Grigoriev (University of Tulsa).

References

1. M. Sucheá, S. Christoulakis, N. Katsarakis, T. Kitsopoulos and G. Kiriakidis, *Thin Solid Films*, 515, 6562-6566 (2007)
2. A. E. Jimenez-Gonzalez, *Journal of Solid-State Chemistry*, 28,176-180 (1997)
3. Y. Cao, L. Miao, S. Tanemura, M. Tanemura, Y. Kuno, Y. Hayashi and Y. Mori, *J. Appl. Phys.*, 45, 1623-1628 (2006)
4. S. H. Mohamed, H. M. Ali, H. A. Mohamed, A. M. Salem, *Eur. Phys. J. Appl. Phys.*, 31 95-99 (2005)
5. A. E. Jimenez-Gonzalez, J. A. S. Urueta, R. Suarez-Parra, *J. Cryst. Growth*, 192, 430 (1998)
6. W. W. Wenas, A. Yamada, A. Yamada, M. Konagai, K. Takahashi, *Jpn. J. Appl. Phys.* 30, L441 (1991)
7. H. W. Lee, S. P. Lau, Y. G. Wang, K. Y. Tse, H. H. Hng, B. K. Tay, *J. Cryst. Growth*, 268, 596 (2004)
8. P. Hari and D. Spencer, *Advances in Science and Technology*, 54, 305-310 (2008)
9. P. Hari, M. Baumer, W. Tennyson and L. A. Bumm, *Non-Crystalline Solids*, 354/19-25, 2843 (2008)
10. P. Hari and D. Spencer, *Phys. Status Solidi C6*, 51, 8150-8153 (2009)
11. P. Hari , M. Byrczek , D. Teeters , and P. Utekar, *International Journal of Nano Physics*, 10, 1, 1-5 (2010)
12. P. Hari, D. Spencer, A. Hor, H. Liang, K. Roberts, K. and D. Teeters *Phys. Status Solidi C*, 8, 2814-2817 (2011)
13. P. Hari, K. Farmer and K. P. Roberts., *Advances in Science and Technology*, 77, 280-284 (2012)
14. T. Athauda, P. Hari and R. Ozer, *Applied Materials and Interfaces*, 5 (13) , 6237-6246 (2013)
15. K. Farmer , P. Hari, and K. P. Roberts, *Canadian Journal of Physics*, 92, 848-841 (2014)
16. M. M. Abd El-Raheem, Ateyah M. Al-Baradi, A. M. A. Amry, E. Abd Elwahab, H. E. A. El-Sayed, S. A. Amin, H. H. Al-Ofri, *Adv. in Materials and Corrosion*, 1, 14-21 (2011)
17. L. Vayssieres, *Adv. Materials*, 15 (5), 464-466 (2003)
18. T. Tsuchiya, T. Emoto, T. Sei, *J. Non-Cryst. Solids* 178, 327 (1994)
19. M. De la, L. Olvera, A. Maldonado, R. Asomoza, M. Melendez-Lira, *Sol. Energy Mater, Sol. Cells* 71, 61(2002)
20. Sha Wang, Ping Li, Hui Liu, Jibiao Li and Yu Wei, *Journal of Alloys and Compounds*, 505, 362-366 (2010)
21. Thid Win, Than Than Win, Yin Muars Muang and Ko Ko Kya Soe, *PCO Proceedings Vol. 2008*, ISBN -979-983-4483-63 (2013)
22. R. Eliarassi and G. Chandrasekharan, *Materials Science in Semiconductor Processing*, 14, 179-183 (2011)
23. S. Baruah, and J. Dutta, *Sci. Technol. Adv. Mater.* 10, p.013001 (2009)
24. V. Assuncao, E. Fortunato, A. Marques, H. Aguas, I. Ferreira, M. E. V. Costa, and R. Martins, *Thin Solid Films* 427, p. 401 (2003)
25. K. Ueda, H. Tabata, and T. Kawai, *Appl. Phys. Lett.* 79, p.988 (2001)
26. H. J. Lee, S. Y. Jeong, C. Cho, and C. Park, *Appl. Phys. Lett.* 81, 4020 (2002)

27. J. J. Chen, M. H. Yu, W. L. Zhou, K. Sun, and L. M. Wang, *Appl. Phys. Lett.* 87, p.5173119 (2000)
28. W. Baiqi, S. Xudong, F. Qiang, J. Iqbal, L. Yan, F. Honggang, and Y. Dapeng, *Physica E* 41, p.413 (2009)
29. A. Singh and H. L. Vishwakarma, *Inter. Journal of Material Physics and Chemistry*, Vol. 1, No. 2, 163-167 (2015)
30. P. Singh, A. Kaushal and D. Kaul, *Jour. of Alloys and Compounds*, 47, 11-15 (2009)
31. M. Boulouddeine, N. Viart, S. Colis, and A. Dinia, *Chem. Phys. Lett.*, 397, 73 (2004)
32. R. He, R. Hocking and T. Tsuzuki, *Materials Chemistry and Physics*, 132, 1035-1040 (2012)
33. V. Gandhi, R. Ganesan, H. H. A. Syedahmed, and M. Thaiyan, *Journal of Physical Chemistry*, 118, 9715-9725 (2014)
34. N. Bahadur, A. K. Srivastava, S. Kumar, M. Deepa and B. Nag, *Thin Film Solids*, 518, 5257-5284 (2010)
35. N. Sabri, A. K. Yahya, and M. Talari, *Volume 132, (7)*, 1735–1739 (2012)
36. G. T. Wright, *Solid State Electronics*, 2, 165-189 (1961)
37. H. C. Card and E. H. Rhoderick, *J. Phys. D: Appl. Phys.* 4, 1589 (1971)
38. S. Sharma and C. Periswamy, *Superlattices and Microstructure*, 72, 12–21 (2014)
39. S. Al-Heniti, R. I. Badran, A. A Al-Ghamedi, F. A. Al-Agel, *Advanced Science Letters*, 4, 1, 23-28 (5) (2011)
40. R. Yatskiv, V. V. Brus, M. Verde, J. Grym, P. Gladkov, *Carbon* 77, 1011-1019 (2014)
41. I. Hussain, M. Y. Soomro, N. Bano, O. Nur and M. Willander, *J. Appl. Phys.* 112, 064506 (2012)
42. M. S. Samuel, J. Koshy, A. Chandran, and K.C. George, *Current Applied Physics*, 11, 1094-1099 (2011)
43. M. S. Samuel, J. Koshy, A. Chandran, and K.C. George, *Physica B*, 406, 3022-3029 (2011)
44. *Impedance Spectroscopy Theory, Experiment, and Applications Second Edition* Edited by E. Barsoukov J. Macdonald, Wiley Interscience (2005)
45. M. R. Abdullah and A. N. Yousoff, *J. Mater. Sci*, 32, 5817-5823 (1997)
46. K. S. Cole and R. H. Cole, *J. Chem. Phys.*, 9, 341-352 (1941)